

Three-dimensional surface strain sensor based on PDMS/LIG composite film with adjustable electromechanical performance

Yang, Huiru; Huang, Qianming; Wang, Shaogang; Zong, Qihang; Tan, Chunjian; Ye, Huaiyu; Zhang, Guoqi

DOI

[10.1016/j.apsusc.2024.159885](https://doi.org/10.1016/j.apsusc.2024.159885)

Publication date

2024

Document Version

Final published version

Published in

Applied Surface Science

Citation (APA)

Yang, H., Huang, Q., Wang, S., Zong, Q., Tan, C., Ye, H., & Zhang, G. (2024). Three-dimensional surface strain sensor based on PDMS/LIG composite film with adjustable electromechanical performance. *Applied Surface Science*, 660, Article 159885. <https://doi.org/10.1016/j.apsusc.2024.159885>

Important note

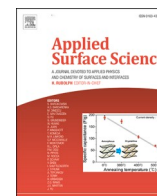
To cite this publication, please use the final published version (if applicable). Please check the document version above.

Copyright

Other than for strictly personal use, it is not permitted to download, forward or distribute the text or part of it, without the consent of the author(s) and/or copyright holder(s), unless the work is under an open content license such as Creative Commons.

Takedown policy

Please contact us and provide details if you believe this document breaches copyrights. We will remove access to the work immediately and investigate your claim.



Full Length Article

Three-dimensional surface strain sensor based on PDMS/LIG composite film with adjustable electromechanical performance

Huiru Yang^{a,b}, Qianming Huang^{a,b}, Shaogang Wang^c, Qihang Zong^b, Chunjian Tan^c,
Huaiyu Ye^{b,*}, Guoqi Zhang^c

^a Harbin Institute of Technology, Harbin 150001, China

^b School of Microelectronics, Southern University of Science and Technology, Shenzhen 518055, China

^c Faculty of EEMCS, Delft University of Technology, Mekelweg 4, 2628 CD Delft, the Netherlands

ARTICLE INFO

Keywords:

PDMS/LIG composite

Strain sensor

3D surface sensing

Adjustable electromechanical performance

ABSTRACT

Flexible strain sensors play a crucial role in health monitoring, smart wearable devices, and human-machine interaction. Three-dimensional surface evaluation methods for strain sensors offer advantages by being closer to actual strain, featuring a larger working range, and being more suitable for multidirectional strain. In this study, a three-dimensional (3D) surface strain sensor based on polydimethylsiloxane/laser-induced graphene (PDMS/LIG) composite films has been developed. The electromechanical properties of this sensor, encompassing 3D strain range and sensitivity, can be adjusted by manipulating laser parameters and LIG patterns. The key to attaining these specific characteristics lies in the intentional design of crack types and orientations on the sensor's surface. Remarkably, the line-vertical (LV) sensor exhibits outstanding sensitivity with a GF of 211.3. The line-parallel (LP) sensor achieves a GF of 115.1. Additionally, it demonstrates a stretching range of 25% and maintains stable performance over an extensive number of strain/release test cycles (more than 3000 cycles). With these advantages, the 3D strain sensor can not only be applied in human activity monitoring but also monitoring pressure within microchannels in microfluidic chips, suggesting promising applications in the health and medical fields.

1. Introduction

Flexible strain sensors, which transduce mechanical deformations into electrical signals, play a crucial role in health monitoring[1,2], smart wearable devices[3], and human-machine interaction[4,5]. The electromechanical characteristics of strain sensors determine their potential applications, making accurate assessment of these characteristics crucial. To date, the majority of reported methods for testing strain sensors have been confined to two-dimensional (2D) evaluations [6,7]. However, in practical sensor applications involving human motion detection, relying solely on meeting sensing requirements in two dimensions while neglecting changes in three-dimensional (3D) surfaces can significantly impact the accuracy of motion detection [8–11]. Consequently, current methods for testing strain sensor performance in human motion detection applications do not comprehensively capture the 3D sensing mechanism, presenting a challenge in determining the 3D surface sensing performance of various strain sensors.

To address this challenge, numerous researchers have explored the

bidirectional tensile deformation[12,13] and bending deformation [14–16] of sensors. However, there has been limited focus on 3D sensing performance. Li et al. [17] proposed an innovative method for evaluating the sensing performance of knitted strain sensors using a 3D curved surface. The results suggest that, compared to 2D testing methods, the 3D testing approach closely aligns with the actual human sensing situation. However, the application of this method in other strain sensors remains unexplored. To overcome the limitations of current flexible thin-film strain sensors in 3D surface monitoring, this work employs the 3D surface testing method to evaluate the stretching range and sensitivity of strain sensors, providing insights into their authentic deformation and response within a three-dimensional context.

Additionally, sensitive materials play a crucial role in strain sensors, and their performance directly affects the sensor's sensitivity, stability, and reliability. Currently, extensively researched sensitive materials include graphene[2,18,19], carbon nanotubes (CNTs)[20–22], MXene [23–25], conductive polymers[26–28], metal nanomaterials[29–31], and their composite materials[32–34]. Graphene and its derivatives

* Corresponding author.

E-mail address: yehy@sustech.edu.cn (H. Ye).

<https://doi.org/10.1016/j.apsusc.2024.159885>

Received 18 December 2023; Received in revised form 20 February 2024; Accepted 11 March 2024

Available online 13 March 2024

0169-4332/© 2024 Elsevier B.V. All rights reserved.

have been widely studied due to their excellent flexibility, conductivity, and mechanical strength. Among them, laser-induced graphene (LIG) [35,36] has attracted widespread interest due to its simple preparation and unique porous structure. LIG has been successfully applied in various sensors [37–39], particularly in strain sensors, yielding significant advancements in fields such as wearable electronics [40] and motion monitoring [41].

Despite the considerable progress made in LIG strain sensors, challenges still exist and need urgent attention. One of the primary challenges is striking a balance between sensitivity and strain range. Current solutions focus on designing microstructures and implementing material modifications to address this issue. For instance, Park et al. [42] enhanced the sensitivity and reliability of resistive strain sensors by employing MoS₂-modified LIG. Liu et al. [43] utilized laser technology to synthesize graphene films embedded with Pt nanoparticles in situ, resulting in wearable strain sensors with ultra-high sensitivity and stability. Xie's research group devised a fingerprint-inspired strain sensor [10] based on LIG to optimize sensitivity and strain range. Additionally, they developed a scorpion-inspired dual-bioinspired microcrack-assisted wrinkled LIG/Ag strain sensor [44], exhibiting high sensitivity and a broad working range. However, these solutions often involve intricate processing steps, increasing costs and potentially limiting practical applications. Therefore, this work proposes a method to control the sensitivity of LIG strain sensors through pattern design. By designing surface patterns, improvements in sensor performance can be achieved without adding complexity to the manufacturing process.

In this work, the 3D surface strain monitoring method is introduced into flexible thin film strain sensors to improve their applicability in health monitoring. PDMS/LIG composite films were prepared by transfer method, and stable electromechanical properties were obtained. Different laser process parameters and various LIG patterns were designed, and their impact on electromechanical performance was investigated to optimize the performance of LIG strain sensors for complex applications. This research aims to overcome the current limitations of flexible strain sensors in terms of performance and provide a more reliable and efficient solution for health monitoring in the future.

2. Experimental section

2.1. Fabrication of LIG

The laser processing employed in the fabrication of laser-induced graphene (LIG) is performed under ambient conditions, with the polyimide (PI) tape attached to the copper substrate using its adhesive sides. This procedure utilizes a CO₂ laser system (HSC30-E, Han's Laser Technology Industry Group Co., Ltd., wavelength: 10.6 μm). The operation is conducted at a constant scanning speed of 50 mm/s, with the laser's average power ranging from 1 % to 11 %, and a laser pulse repetition frequency of 1–8 kHz. These parameters are investigated to assess their impact on the surface morphology and composition of the graphene generated through laser irradiation.

2.2. Fabrication of 3D surface strain sensor

The fabrication process of the strain sensor based on PDMS/LIG composite films. By adjusting various laser parameters and designing various patterns, LIG with distinct electromechanical characteristics can be produced. The laser scanning speed is consistently set at 50 mm/s, and the line spacing is configured at 0.25 mm. Following the generation of LIG, a liquid mixture of PDMS (Polydimethylsiloxane) precursor (Sylgard 184, Dow Corning, mixture ratio: 10:1) undergoes degassing in a vacuum chamber. This mixture is then spin-coated onto the LIG surface using a spin coater (WH-SC-01, Wenhao Co., Ltd., spin parameters: 300 rpm, 30 s + 500 rpm, 20 s) and cured at 80 °C for 2 h. Subsequently, the PI layer is peeled off, and LIG is transferred onto PDMS, resulting in a PDMS/LIG composite film with a thickness of 160 μm. Silver paste is

applied to connect the LIG electrodes with copper wires, followed by drying in an 80 °C oven for 15 min. Finally, the PDMS mixture is poured into the electrode connection area, completing the final encapsulation of the strain sensor.

2.3. Characterization of LIG

The surface morphology of LIG and PDMS/LIG films was characterized using a scanning electron microscope (SEM, ZEISS Gemini 300) and optical microscope (OM, OLYMPUS BX53M). A 3D laser scanning microscope (KEYENCE VK-X1000) was employed to observe the three-dimensional morphology of LIG. Raman spectra were acquired by exciting the samples with a 532 nm laser using LabRAM HR Evolution (HORIBA).

2.4. Measurement of 3D surface strain

To investigate the response of sensors to 3D surface strain, a dedicated 3D surface strain testing platform was established. The mechanical performance of 3D surface strain sensors was assessed using a universal testing machine (TSE503A, Vance Testing Machine Co., Ltd.). Simultaneously, a digital multimeter (DAQ6510, Keithley) was employed to synchronously test and collect real-time resistance signals from the sensors.

Fig. 1b illustrates the schematic diagram depicting the location of the 3D strain test. Following the methods outlined by Pei [45] and Li [17], the average strain of the sensor in a random direction, ε , is defined by equation (1). This method is adapted for the 3D strain characterization of flexible PDMS/LIG films.

$$\varepsilon = \frac{L + S - R}{R} \times 100\% \quad (1)$$

Here, $R = 5$ mm represents the inner diameter of the sensitive film, and L is the tensile length of the film without contact with the steel ball, determined by equation (2):

$$L = \sqrt{(D - r)^2 + R^2 - r^2} \quad (2)$$

Where D is the depth of the compressed film of the steel ball, and $r = 4$ mm is the radius of the steel ball. S represents half of the arc length when the steel ball comes into direct contact with the thin film, expressed as equation (3):

$$S = r \left(\tan^{-1} \frac{r}{L} + \tan^{-1} \frac{D - r}{R} \right) \quad (3)$$

3. Results and discussion

3.1. Fabrication and characterization

For flexible 3D surface strain sensors, unlike the planar stretching of two-dimensional strain sensors, it is essential to perform curvature stretching on the thin film. Hence, the establishment of a 3D strain testing platform and the calibration of 3D strain are of paramount significance. Fig. 1a illustrates the schematic diagram of the preparation of PDMS/LIG 3D surface strain sensors and the principal diagram of 3D stretching performance testing. The 3D strain sensor is circularly shaped and affixed to a circular hole. 3D deformation of the sensor's surface is induced by vertically pressing a steel ball onto it. The corresponding relationship between the vertical pressing distance (D) and three-dimensional strain (ε) is established to characterize the sensor's three-dimensional strain, as shown in Fig. S1b (the 3D strain characterization method is detailed in the Experimental Section).

The manufacturing process of the sensors involves laser reduction, resulting in LIG with a porous structure on the PI surface. To enhance stretching performance, it is then transferred onto PDMS, a stretchable

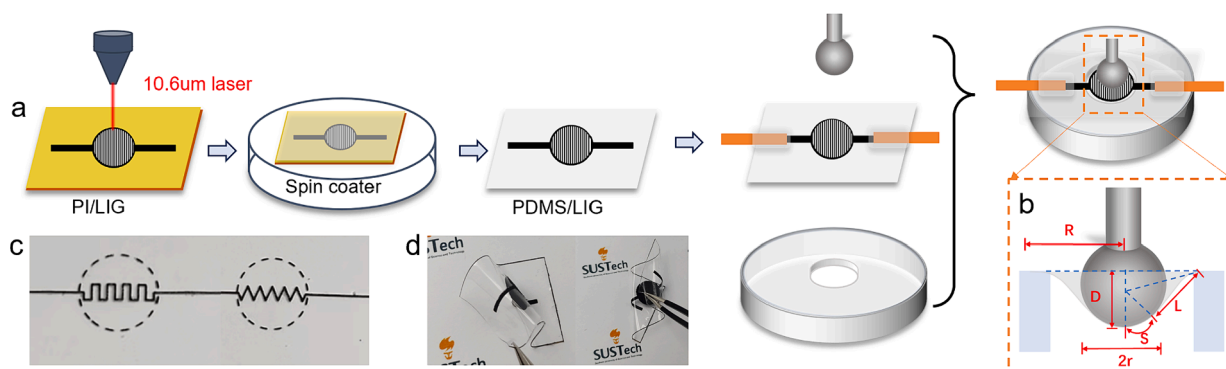


Fig. 1. (a) Schematic diagram of the preparation process for three-dimensional surface strain sensors and the three-dimensional strain testing platform. (b) Characterization method for three-dimensional strain. Establishing the relationship between the vertical descent distance and three-dimensional strain. (c-d) Physical images of the three-dimensional strain sensor, showcasing the ability to design patterns in the sensor's sensitive area, with the sensor possessing flexibility, bendability, and stackability.

and transparent substrate (specific steps are detailed in the Experimental Section). By spin-coating PDMS on the surface of LIG and leveraging its excellent fluidity, the porous structure of LIG is filled. Following PDMS curing, the PI is peeled off to yield a PDMS/LIG flexible composite film. By adjusting spin-coating parameters, PDMS/LIG composite films with varying thicknesses can be produced. In this work, PDMS/LIG films with an approximate thickness of 160 μm were prepared. The physical image of a 3D strain sensor is presented in Fig. 1c-d, showcasing the ability to design patterns in the sensitive area of the sensor. Furthermore, the sensor exhibits flexibility, bendability, and stackability.

Previous studies have indicated that laser parameters, including laser repetition frequency, average power, scanning speed, and working distance, have a significant impact on LIG[46,47]. To investigate the influence of different laser parameters on the formation and surface morphology of LIG, this section explores the effects of laser average power (P_{avg}) and repetition frequency (f) on LIG through characterization of the product's surface morphology, and Raman spectra.

Fig. 2a depicts the surface morphology of LIG produced under varying laser parameters. It is evident that, within each row, with a

consistent laser scanning speed ($v = 50 \text{ mm/s}$) and repetition frequency, insufficient laser average power results in the failure to form LIG, while excessively high average power may lead to damage on the polyimide surface. Moreover, laser repetition frequency proves to be a critical parameter influencing surface morphology. Looking at each column, maintaining a constant laser scanning speed and average power, a reduction in repetition frequency amplifies the degree of sample surface ablation. This phenomenon can be characterized by the single-pulse laser energy ($E_{sp} = P_{avg}/f$), as shown in Fig. 2b, where an increase in E_{sp} leads to a greater laser ablation depth on the PI surface, thereby affecting surface morphology.

The area delineated by the red box in Fig. 2a represents the selected region with completely carbonized and intact surface samples. Their Raman spectroscopy confirms the formation of LIG, as depicted in Fig. 2c. The presence of D, G, and 2D bands aligns with the characteristic features of typical LIG produced by laser irradiation of PI films, as reported previously[12,47]. The peak at 1580 cm^{-1} (G-band) signifies the primary phonon arising from lattice stretching in the C – C bonding within the graphitic plane. The D-band observed at about 1350 cm^{-1}

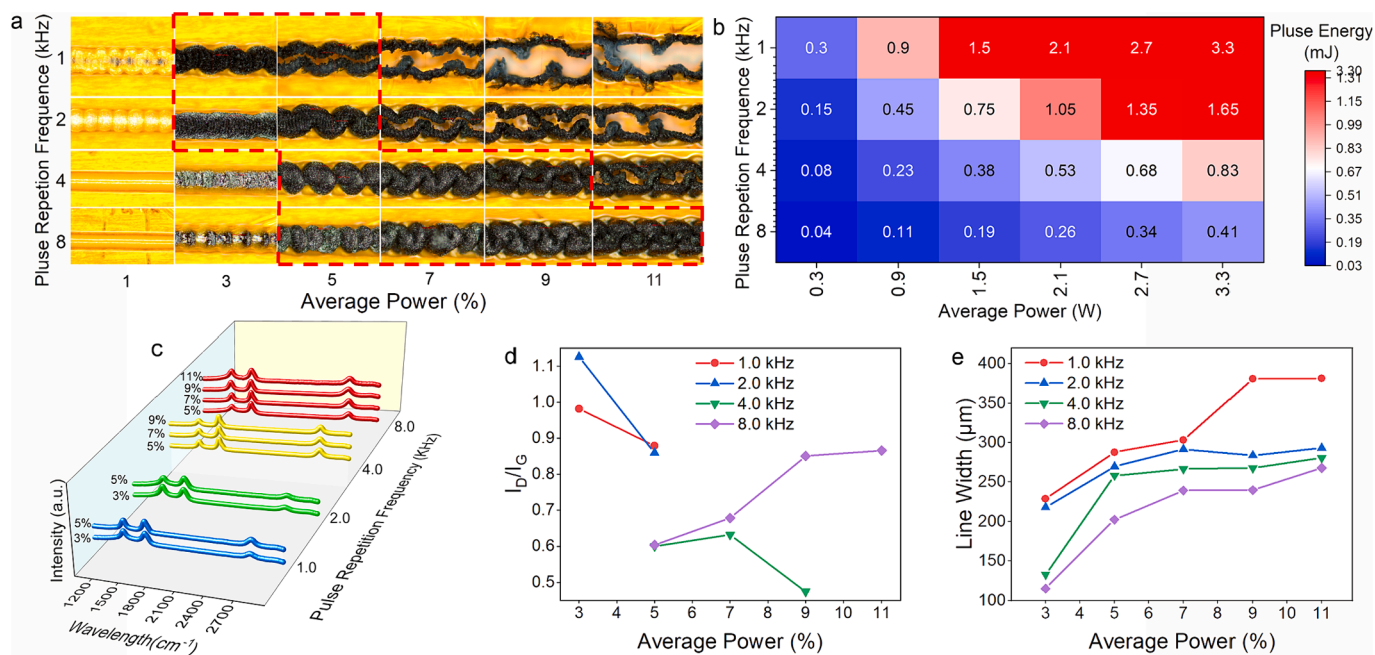


Fig. 2. Impact of diverse laser parameters on the morphology and quality of LIG. (a) Optical microscopy images of LIG with different laser parameters. (b) Respective E_{sp} values for different laser parameters. (c) Raman spectra of the selected area under different laser parameters. (d) I_D/I_G ratios under different laser parameters. (e) Line width variations under different laser parameters.

corresponds to the disorder and defects in the graphitic lattice. The 2D band results from a secondary phonon vibration of the C – C bonding, providing information about the stacking layers in the carbonized material (such as graphene, and CNT)[48]. The ratio of peak intensity (I_D/I_G) between the D and G bands is a parameter used to quantify the amount of defects in the graphitic material. Fig. 2d illustrates the relationship between laser parameters and I_D/I_G . Under the same laser pulse repetition frequency, an increase in laser average power leads to a decrease in defect density. Particularly, at 4 k-5 %, 4 k-7 %, and 4 k-9 %, LIG exhibits significantly lower defects compared to other parameters. Additionally, the ratio between the 2D and G bands ($I_{2D}/I_G = 0.5 \sim 0.7$) indicates that the graphitic material is composed of multilayer graphene layers[49,50]. Furthermore, the impact of different laser parameters on line width was investigated, as depicted in Fig. 2e. Maintaining a constant laser pulse repetition frequency, an increase in laser average power results in a wider line width. Conversely, keeping the laser average power constant, an increase in laser repetition frequency leads to a narrower line width. This indicates a direct proportionality between line width and E_{sp} , with larger E_{sp} values resulting in wider lines. Consequently, laser parameters play a significant role in shaping the surface morphology, determining the defect amount, and influencing the line width of LIG. At 4 k-5 %, 4 k-7 %, and 4 k-9 %, LIG demonstrates fewer defects and narrower line widths, primarily differing in surface morphology. To further explore the impact of laser parameters on the performance of the strain sensor, these three laser parameters were selected to fabricate sensors for subsequent performance studies.

3.2. Electromechanical performance and mechanism

3.2.1. Performance with different laser parameters

Through the established 3D surface strain testing platform, the sensitivity and stretching range of 3D surface strain sensors prepared under different laser parameters were investigated. The laser parameters

were set as follows: the same laser pulse repetition frequency ($f = 4$ kHz) and scanning speed ($v = 50$ mm/s), with different laser average powers ($P_{avg} = 5\%$, 7% , 9%). The prepared sensors were labeled as P5, P7, and P9. Their responses to strain are shown in Fig. 3a. P5 exhibits higher sensitivity than P7 and P9 but with a narrower stretching range. P7 and P9 show similar sensitivities within 20 % stretching ranges. To elucidate the mechanism by which different laser parameters affect the performance of 3D strain sensors, the stress distribution of the sensors under three-dimensional tensile strain was studied through finite element analysis, as depicted in Fig. 3b. Stress decreases radially from the center. The laser paths of P5 and P9 sensors were consistent, as shown in Fig. 3c, and three locations were selected for SEM characterization, including the center (①), horizontal radius edge (②), and vertical radius edge (③).

After stretching, the surface morphology of P5 is shown in Fig. 3d. At position ②, parallel cracks (red dashed lines indicating cracks parallel to the horizontal direction) appear on the LIG surface; at position ③, vertical cracks (white dashed lines indicating cracks perpendicular to the horizontal direction) form at the interface between LIG and PDMS; at position ①, both types of cracks are observed. This is because when the surface of the 3D strain sensor is stretched, the force is applied along the radial direction, causing cracks to form at positions perpendicular to the force (radius) direction. Therefore, cracks at positions ② and ③ exhibit a single direction, and the crack direction is entirely perpendicular to the force (radius) direction. At position ①, the applied tensile force comes from all directions, resulting in cracks in different directions. Based on characterization results, the equivalent circuit schematic of P5 is shown in Fig. 3e, equivalent to resistors in series with different resistances. When strain is applied to its surface, the formation of parallel cracks leads to a change in resistance, while vertical cracks hardly affect resistance variation. This is because parallel cracks are perpendicular to the current direction, and their formation and enlargement hinder the flow of current, increasing resistance. Since only cracks in a single

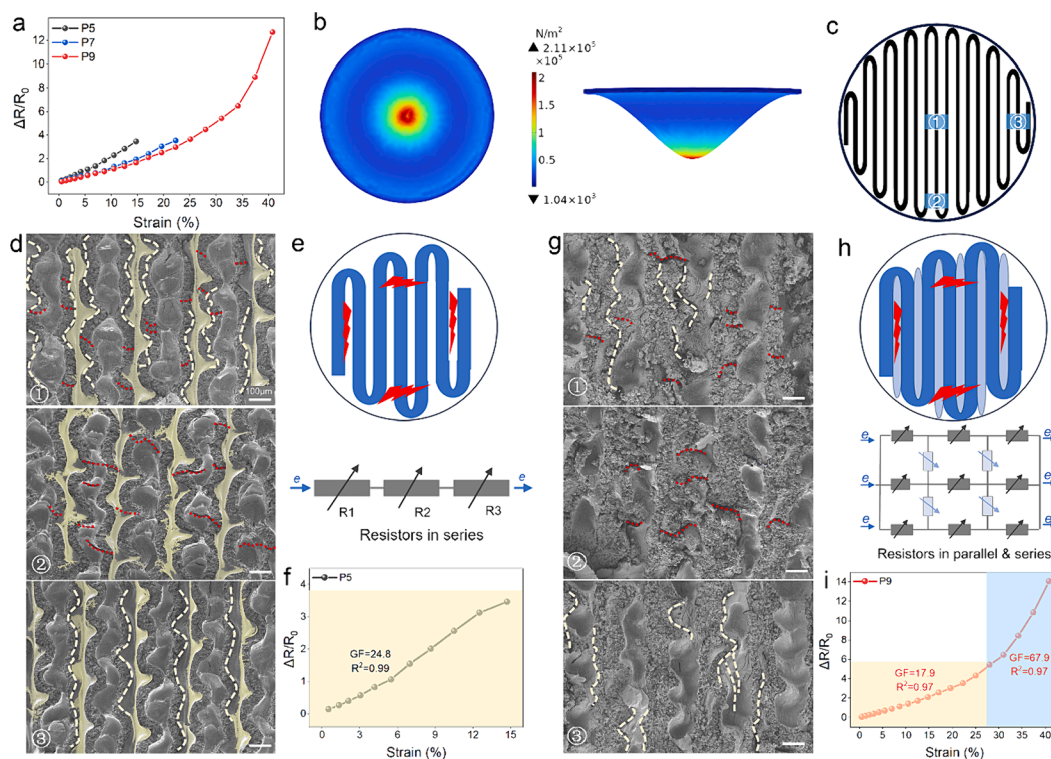


Fig. 3. Electromechanical characteristics and mechanism of 3D strain sensors with different laser parameters. (a) Influence of different laser parameters on the electromechanical characteristics. (b) Stress distribution on the surface of the strained thin film was simulated through finite element analysis. (c) Laser paths and characterization positions of the sensor. (d) SEM images of P5. (e) Equivalent circuit model of P5. (f) Electromechanical characteristics of P5. (g) SEM images of P9. (h) Equivalent circuit model of P9. (i) Electromechanical characteristics of P9.

direction (channel cracks) affect circuit resistance, the response of P5 to strain exhibits good linearity and sensitivity. However, as cracks enlarge, the circuit will be completely disconnected, resulting in infinite resistance and a limited measurable strain range, as shown in Fig. 3f.

Similarly, SEM characterization was performed on the surface morphology of P9 at the same three different positions, as shown in Fig. 3g. Its surface does not have a separate PDMS layer because P9 has a larger line width than P5, preventing PDMS from infiltrating its surface. SEM indicates that parallel and vertical cracks appear at positions ② and ③ on the LIG surface, respectively, while both types of cracks are observed at position ①. Similarly, the crack direction is perpendicular to the force direction. The equivalent circuit schematic is shown in Fig. 3h, equivalent to a series-parallel circuit. When strain is applied to its surface, both parallel and vertical cracks affect resistance changes. Due to the combined action of these two types of cracks (network cracks), P9 can monitor a wider strain range, but the sensitivity decreases, as shown in Fig. 3i. These results reflect the trade-off between sensitivity and strain range, consistent with literature findings [51,52].

The above-mentioned analysis indicates that 3D strain sensors, when subjected to surface strain, develop cracks on the surface perpendicular to the direction of radial, as the force is applied along the radial direction. In different circuit models, cracks in different directions have varying effects on resistance. Specifically, resistance is primarily influenced by cracks perpendicular to the direction of the current flow. Based on their impact on resistance, cracks can be broadly categorized into two types: channel cracks (having a single direction, mainly affecting sensitivity) and network cracks (possessing multiple directions, primarily influencing the stretching range). In P5, cracks are predominantly channel cracks, resulting in better linearity and sensitivity but a smaller stretching range. In contrast, in P9, cracks are mainly network cracks, leading to a wider stretching range but a reduction in sensitivity.

This aligns with findings in the literature[31,53]. Consequently, by designing the crack distribution and type, it is possible to manipulate the electromechanical characteristics of the sensor.

3.2.2. Performance with different patterns

In this section, the impact of different LIG patterns on the tensile range and sensitivity of 3D strain sensors was systematically investigated. Various patterns, including sector, linear patterns in different scanning directions (parallel and vertical), and grid, were designed and labeled as Sector, LP (Line parallel), LV (Line vertical), and Grid, as shown in Figure S5a. The design principles of different patterns in the sensitive area of sensors and the specific parameters of each pattern are described in Supporting Information (Figure S6).

The resistance change rates of these sensors concerning strain are depicted in Fig. 4, showing their 3D strain ranges and gain factors (GF). The results suggest that, in comparison to the P9 sensor, all the aforementioned sensors demonstrate enhanced sensitivity, albeit with a reduction in the maximum tensile range. The P9 sensor exhibits the broadest tensile range, reaching 40%. In the 0–28% tensile range, the corresponding GF is 17.9, while in the 28–40% range, the GF can reach 67.9. The LV sensor stands out with the highest sensitivity (GF = 211.3) but a relatively limited strain range of only 7%. The Sector sensor achieves increased sensitivity in the 0–28% tensile range, reaching 28.5. Despite a decrease in tensile range to around 20% compared to P9, the Grid sensor shows an increase in sensitivity (GF ≈ 31.3). The LP sensor demonstrates a GF of 34.9 in the 0–20% tensile range and a GF of 115.1 in the 20–25% tensile range. This indicates that the sensor excels in balancing a large tensile range (up to 25%) with high sensitivity (GF_{max} = 115.1).

The variances in electromechanical characteristics among different pattern sensors can be explained through the crack mechanism

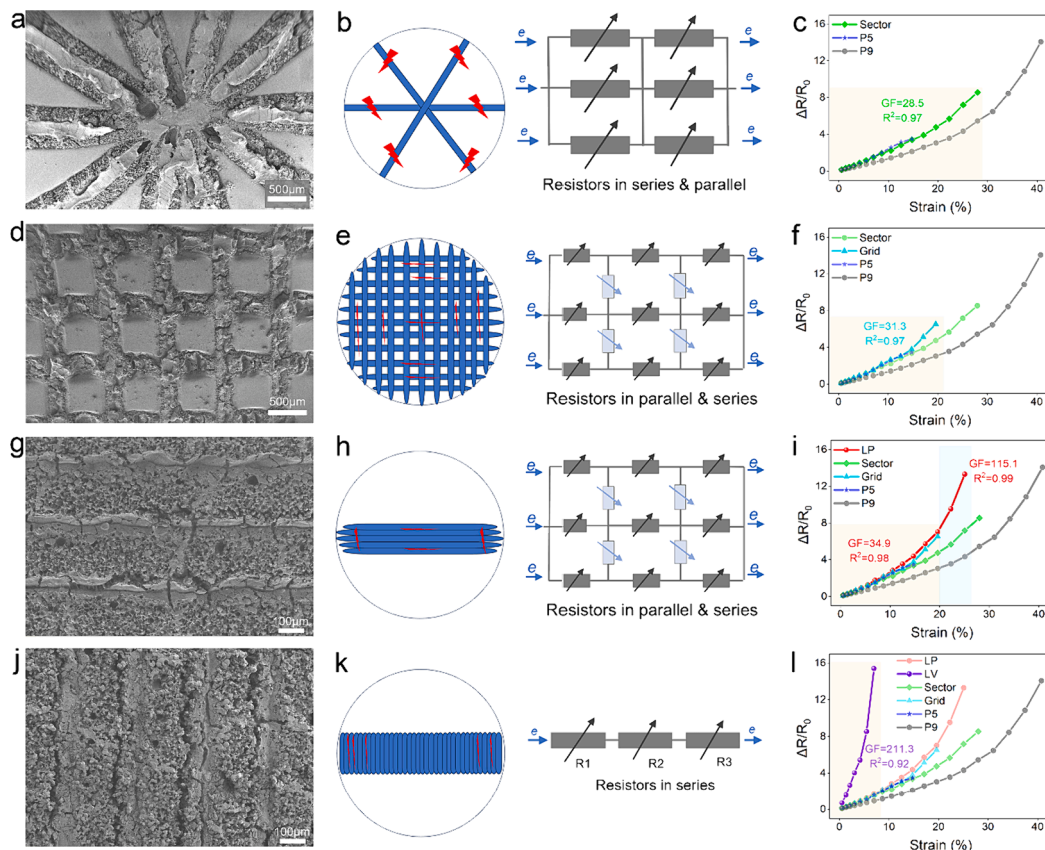


Fig. 4. Electromechanical characteristics and mechanism of 3D strain sensors with different LIG patterns. SEM images of surface morphology, equivalent circuit model, electromechanical characteristics of (a-c) Sector sensor, (d-f) Grid sensor, (g-i) LP sensor, (j-l) LV sensor.

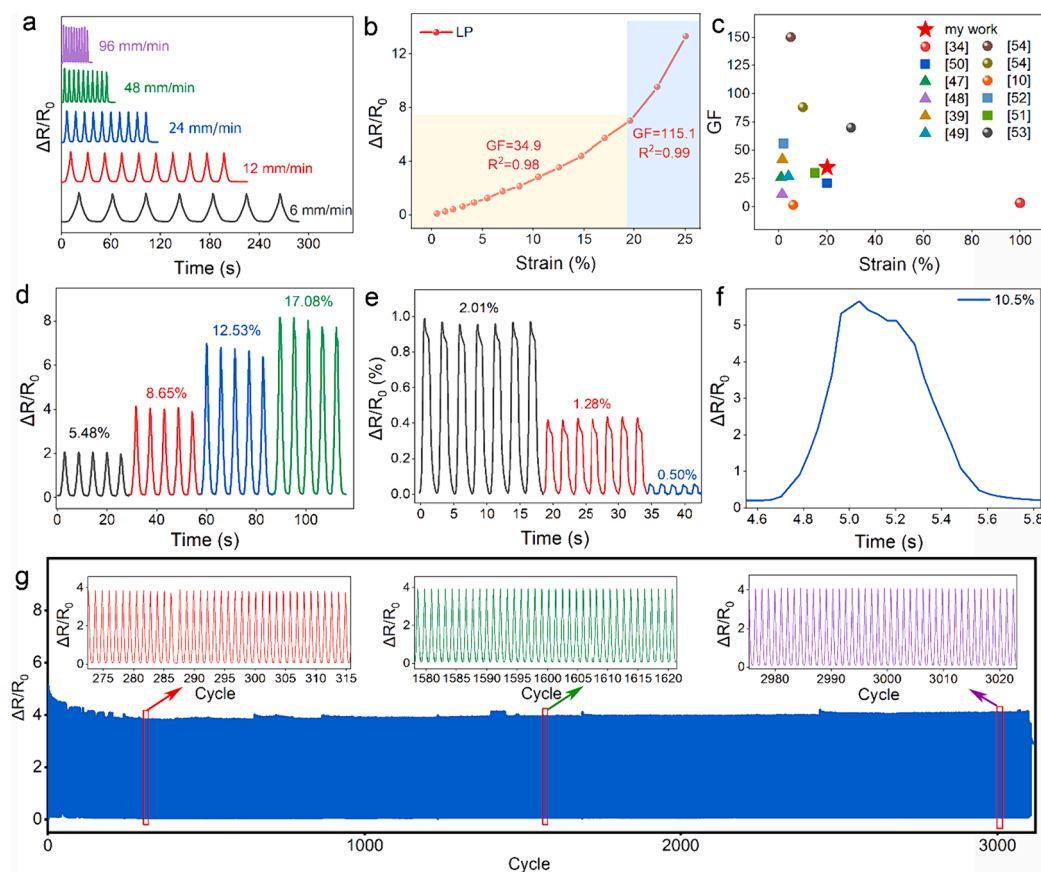


Fig. 5. Electromechanical characteristics of LP sensors. (a) The influence of tensile frequency on response. (b) The change in resistance rate with strain. (c) Comparison of tensile range and GF with literature. (d) Dynamic response at larger strains (5%–17%). (e) Response at smaller strains, with a minimum detectable strain of 0.50%. (f) Response time and recovery time. (g) Tensile-release cycling over 3000 cycles.

mentioned earlier. Regarding the Sector sensor, the designed LIG is along different radial directions and parallel to the force direction. When subjected to 3D surface strain, the surface generates cracks all perpendicular to the radius, as shown in Fig. 4a, confirming the previously mentioned theory that crack direction is perpendicular to the force direction. The schematic diagram of Sector sensor surface morphology and its equivalent circuit model, as shown in Fig. 4b, where crack direction is all perpendicular to the current direction, is the main factor affecting resistance change. Due to the influence of only a single type of crack (channel crack), the Sector sensor exhibits a linear response (Fig. 4c). Compared to P5, the design of parallel conductive pathways effectively enhances the tensile range. The designed LIG of Grid sensor is distributed horizontally and vertically. After the sensor surface is subjected to 3D strain, cracks occur in different directions, as shown in Fig. 4d. Its schematic diagram of surface morphology and circuit model, as shown in Fig. 4e, is similar to P9, where both vertical and horizontal cracks affect resistance to change; the difference lies in the change in the conductive network density. The Grid sensor's decreased network density results in a more pronounced change in resistance under the same strain. Therefore, compared to P9, the Grid sensor's sensitivity effectively increases, but at the cost of reducing the strain monitoring range (Fig. 4f). Regarding the LP sensor, the designed LIG is along the horizontal direction. After subjecting to 3D strain, both vertical and parallel cracks occur simultaneously at the surface center, with vertical cracks dominating closer to the edge, as shown in Fig. 4g. This also aligns with the theoretical assertion that crack direction is perpendicular to the force direction. Its equivalent circuit model, as shown in Fig. 4h, includes two different types of cracks: channel crack (edge) and network crack (center), also similar to the P9 model. The difference lies in the change in the conductive network area; the LP sensor's network area

decreases compared to P9. Under the same strain, the LP sensor's resistance change is more pronounced. Therefore, compared to P9, sensitivity is effectively increased (Fig. 4i). The designed LIG of LV sensor is vertically distributed and has the same strain-sensitive area as the LP sensor. When subjected to 3D strain, cracks mainly occur in the vertical direction, and cracks are mainly formed at the interface of adjacent LIG, as shown in Fig. 4j. When the sensor surface is subjected to tension, the width of the vertical cracks will increase, making the vertical cracks the main cracks in the LV sensor. In the equivalent circuit model, as shown in Fig. 4k, the vertical crack direction is perpendicular to the current direction and is the primary factor affecting the resistance (channel crack). After increasing the strain, vertical cracks are more likely to expand and reach the fracture limit, resulting in the high sensitivity and small strain range of this sensor, presenting a linear response (Fig. 4l). Therefore, the sensitivity and strain range of PDMS/LIG 3D surface strain sensors can be adjusted by controlling LIG patterns. This observation strongly suggests that PDMS/LIG composite films with adjustable designs may be suitable for strain sensors with different sensitivities.

3.2.3. Electromechanical performance of Line-Parallel sensors

To further investigate the dynamic response and reliability of the LP sensor, various tests were conducted including dynamic stretching/release under different stretching ranges, detection limit, response/recovery time, and repeatability, as shown in Fig. 5.

To explore the influence of stretching rate on the sensor response, the impact of different stretching rates under the same strain (8.65%) was first studied, as depicted in Fig. 5a. Within the test speed range of 6–96 mm/min, the effect of different stretching rates on the relative resistance was minimal, contributing to obtaining a reliable response. Fig. 5b

illustrates the functional relationship between the relative change in resistance and strain for the LP sensor. The graph displays the stretching range and GF of the sensor, where GF is calculated as $(\Delta R/R_0)/\epsilon$. The LP sensor demonstrates a GF of 34.9 in the 0–20 % tensile range and a GF of 115.1 in the 20–25 % tensile range. In comparison with recent studies on two-dimensional stretching strain sensors based on LIG, our work exhibits excellent sensitivity within a broad strain range, as shown in Fig. 5c. These studies can be classified into three categories: (i) pure LIG on different substrates such as commercial PI films[54,55], textiles[56], and paper[46]; (ii) LIG on mixtures of LIG precursor materials and flexible materials, such as polyether ether ketone (PEEK)/PDMS[57] and PI/PDMS[58,59]; (iii) LIG transferred from PI films to other substrates, such as medical-grade polyurethane [60], Ecoflex[10], and PDMS [41,61].

Furthermore, to validate the dynamic stretching response of the sensor, periodic stretching/release tests were conducted at 5–17 % strains to verify real-time dynamic processes. The results indicate that within a wide strain range, the sensor exhibits stable and consistent signals (Fig. 5d), and the detection limit was determined by applying a small strain to the sensor. Fig. 5e demonstrates that the sensor can detect cyclic strains of 0.50 % (blue line), 1.28 % (red line), and 2.01 % (black line). The results suggest that under various strain conditions, the relative change in resistance is significant, and complete recovery is achieved upon release. Fig. 5f displays the response time and recovery time of the three-dimensional strain sensor under strain stimulation. Both response time and recovery time are closely related to the stretching and strain release rates. When the sample was stretched at an average strain of 10.5 % with a speed of 420 mm/min, the resistance sharply increased, with a response time of 300 ms. After strain release, the resistance recovered to its original state at a rapid rate (400 ms). The reliability of the sensor is crucial in practical applications. Fig. 5g demonstrates that the strain sensor underwent over 3000 cycles of stretching and releasing at a stretching rate of 48 mm/min and a strain of 8.65 %. Throughout the cycles, it exhibited consistent $\Delta R/R_0$ output. While in the beginning phase of the test, a slight overshoot behavior observed in the sensor after the tensile phase is primarily attributed to the viscoelastic-induced creep behavior of the polymer[7]. The inset in Fig. 5g provides a detailed signal response process during the early, middle, and late stages of the cyclic test, indicating that the response curve and peak values did not show significant changes, affirming the good stability and repeatability of the strain sensor.

3.3. Representative applications for monitoring human activities and microfluidic chip

Given the rapid response, good dynamic response, and stability of the LP sensors, as well as the advantages of 3D surface strain sensors with different patterns, such as easy preparation, adjustable working range, and sensitivity, the one-step fabricated PDMS/LIG 3D surface strain sensor has extensive potential applications in human posture monitoring and rehabilitation training. The PDMS/LIG 3D surface strain sensor can continuously monitor large strains, such as joint movements,

as shown in specific results in Fig. 6. When the LP LIG sensor is attached to the fingers and the fingers are bent to 45° and 90°, the relative resistance increases to a certain value and then recovers when the fingers are straightened again (Fig. 6a). Testing five bending cycles at two different angles shows a rapid and stable response of the resistance signal. The LP sensor can also stably monitor the bending of the wrist (Fig. 6b). All these motion data can be collected to create models for posture calibration, disease prevention, and postoperative recovery. Therefore, they have extensive application value in healthcare, human–machine interfaces, and soft robotics.

On the other hand, the PDMS/LIG sensor, equipped with the capability to monitor 3D surface strain, has advantages that also include achieving miniaturization and pattern customization. Therefore, this sensor can be integrated into a microfluidics chip to monitor the pressure in the channel. Fig. 6c presents the response of the miniaturized strain sensor to different pressure changes, with the inset showing the physical picture of the chip, and the stress-sensitive part in a red circular area (diameter: 2 mm). The results indicate that the sensor can effectively monitor pressures of different magnitudes and provide reliable monitoring within the range of 50 mbar and below. Microfluidics chip is widely used in applications such as cell culture, biological analysis, and drug screening. By monitoring the pressure inside microfluidics chips, insights into cell responses under different flow conditions and evaluations of drug effects in microenvironments can be gained[62]. Therefore, pressure monitoring inside microchannel chips based on this 3D surface strain sensor has potential applications in the biomedical field.

4. Conclusions

In summary, a 3D surface strain sensor based on PDMS/LIG composite films has been designed. The electromechanical properties of this sensor, including the 3D strain range and sensitivity, can be finely adjusted by manipulating laser parameters and LIG patterns. The key to achieving these specific characteristics lies in the deliberate design of the types and orientations of cracks on the sensor's surface. The 3D strain sensor's surface experiences force along the radial direction, with stress decreasing radially from the center to the edges, resulting in cracks forming in the direction perpendicular to the radius. Channel cracks, influencing current flow in a single direction, result in sensors with high sensitivity and good linearity. Conversely, network cracks, affecting current flow from multiple directions, endow sensors with a broader stretching range. Remarkably, the LP sensor with network cracks exhibits outstanding sensitivity, reaching a maximum value of 115.1, coupled with a stretching range of 25 % and stable performance over 3000 cycles. The 3D strain sensor can not only be used for human activity monitoring but also applied to monitor pressure within microchannels in microfluidic chips, suggesting potential applications in the health and medical fields.

CRediT authorship contribution statement

Huiru Yang: Writing – original draft. Qianming Huang:

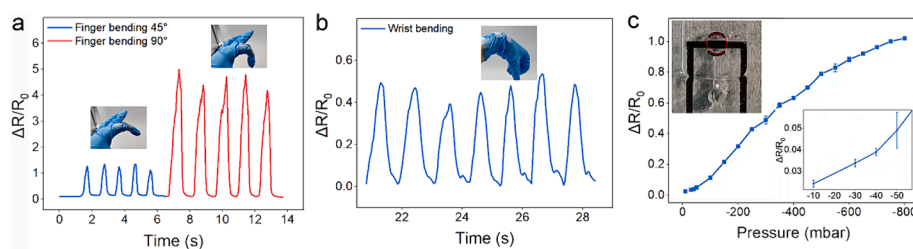


Fig. 6. Applications of the 3D surface strain sensor in human activity monitoring and real-time pressure monitoring in a microfluidic chip. (a) Relative resistance changes of the sensor during finger bending monitoring at different bending angles (45°, 90°). (b) Relative resistance changes of the sensor during wrist bending monitoring. (c) Miniaturized PDMS/LIG sensor integrated into a microfluidic chip for real-time pressure monitoring in its channels.

Investigation. **Shaogang Wang**: Data curation. **Qihang Zong**: Formal analysis. **Chunjian Tan**: Validation. **Huaiyu Ye**: Supervision, Funding acquisition. **Guoqi Zhang**: Resources.

Declaration of competing interest

The authors declare that they have no known competing financial interests or personal relationships that could have appeared to influence the work reported in this paper.

Data availability

Data will be made available on request.

Acknowledgments

This work is supported by the Shenzhen Major Science and Technology Projects (KJZD20230923114710022), Joint Lab of Advanced Situation Awareness, Joint Lab of Advanced Packaging Technology, Joint Lab of Advanced Packaging and Testing Technology of Integrated Circuits.

Appendix A. Supplementary data

Supplementary data to this article can be found online at <https://doi.org/10.1016/j.apsusc.2024.159885>.

References

- Z. Shen, F. Liu, S. Huang, H. Wang, C. Yang, T. Hang, J. Tao, W. Xia, X. Xie, Progress of flexible strain sensors for physiological signal monitoring, *Biosens Bioelectron* 211 (2022) 114298.
- H. Zhang, R. He, Y. Niu, F. Han, J. Li, X. Zhang, F. Xu, Graphene-enabled wearable sensors for healthcare monitoring, *Biosens Bioelectron* 197 (2022) 113777.
- M. Amjadi, K.-U. Kyung, I. Park, M. Sitti, Stretchable, skin-mountable, and wearable strain sensors and their potential applications: A review, *Adv. Funct. Mater.* 26 (2016) 1678–1698.
- S. Pyo, J. Lee, K. Bae, S. Sim, J. Kim, Recent progress in flexible tactile sensors for human-interactive systems: From sensors to advanced applications, *Adv Mater* 33 (2021) e2005902.
- H. Kim, Y.T. Kwon, H.R. Lim, J.H. Kim, Y.S. Kim, W.H. Yeo, Recent advances in wearable sensors and integrated functional devices for virtual and augmented reality applications, *Adv. Funct. Mater.* 31 (2020).
- M. Chao, Y. Wang, D. Ma, X. Wu, W. Zhang, L. Zhang, P. Wan, Wearable MXene nanocomposites-based strain sensor with tile-like stacked hierarchical microstructure for broad-range ultrasensitive sensing, *Nano Energy* 78 (2020).
- A. Chhetry, S. Sharma, S.C. Barman, H. Yoon, S. Ko, C. Park, S. Yoon, H. Kim, J. Y. Park, Black phosphorus@Laser-engraved graphene heterostructure-based temperature-strain hybridized sensor for electronic-skin applications, *Adv. Funct. Mater.* 31 (2020).
- H. Jeon, S.K. Hong, M.S. Kim, S.J. Cho, G. Lim, Omni-purpose stretchable strain sensor based on a highly dense nanocracking structure for whole-body motion monitoring, *ACS Appl Mater Interfaces* 9 (2017) 41712–41721.
- Y. Zhou, P. Zhan, M. Ren, G. Zheng, K. Dai, L. Mi, C. Liu, C. Shen, Significant stretchability enhancement of a crack-based strain sensor combined with high sensitivity and superior durability for motion monitoring, *ACS Appl Mater Interfaces* 11 (2019) 7405–7414.
- W. Wang, L. Lu, Z. Li, L. Lin, Z. Liang, X. Lu, Y. Xie, Fingerprint-inspired strain sensor with balanced sensitivity and strain range using laser-induced graphene, *ACS Appl Mater Interfaces* 14 (2022) 1315–1325.
- Y. Wu, I. Karakurt, L. Beker, Y. Kubota, R. Xu, K.Y. Ho, S. Zhao, J. Zhong, M. Zhang, X. Wang, L. Lin, Piezoresistive stretchable strain sensors with human machine interface demonstrations, *Sens. Actuators, A* 279 (2018) 46–52.
- R. Rahimi, M. Ochoa, W. Yu, B. Ziaie, Highly stretchable and sensitive unidirectional strain sensor via laser carbonization, *ACS Appl Mater Interfaces* 7 (2015) 4463–4470.
- G. Yang, X. Tang, G. Zhao, Y. Li, C. Ma, X. Zhuang, J. Yan, Highly sensitive, direction-aware, and transparent strain sensor based on oriented electrospun nanofibers for wearable electronic applications, *Chem. Eng. J.* 435 (2022).
- K.H. Kim, N.S. Jang, S.H. Ha, J.H. Cho, J.M. Kim, Highly sensitive and stretchable resistive strain sensors based on microstructured metal nanowire/elastomer composite films, *Small* 14 (2018) e1704232.
- C. Liu, S. Han, H. Xu, J. Wu, C. Liu, Multifunctional highly sensitive multiscale stretchable strain sensor based on a graphene/glycerol-KCl synergistic conductive network, *ACS Appl Mater Interfaces* 10 (2018) 31716–31724.
- Q. Li, T. Wu, W. Zhao, J. Ji, G. Wang, Laser-induced corrugated graphene films for integrated multimodal sensors, *ACS Appl Mater Interfaces* 13 (2021) 37433–37444.
- Y. Li, X. Miao, J.Y. Chen, G. Jiang, Q. Liu, Sensing performance of knitted strain sensor on two-dimensional and three-dimensional surfaces, *Mater. Des.* 197 (2021).
- Q. Zheng, J.-H. Lee, X. Shen, X. Chen, J.-K. Kim, Graphene-based wearable piezoresistive physical sensors, *Mater. Today* 36 (2020) 158–179.
- C. Hui, Z. Fengling, Z. Jian, L. Ying, Z. Jinbo, D. Shurong, L. Xuqing, E. Ahmed, D. Huigao, F. Yongqing, Advances in graphene-based flexible and wearable strain sensors, *Chem. Eng. J.* (2023), <https://doi.org/10.1016/j.cej.2023.142576>.
- T. Jian, W. Yuting, M. Shidong, Y. Tao, P. Zhijuan, Flexible strain sensor based on CNT/TPU composite nanofiber yarn for smart sports bandage, *Compos. B Eng.* (2022), <https://doi.org/10.1016/j.compositesb.2021.109605>.
- X. Sun, J. Sun, T. Li, S. Zheng, C. Wang, W. Tan, J. Zhang, C. Liu, T. Ma, Z. Qi, C. Liu, N. Xue, Flexible tactile electronic skin sensor with 3D force detection based on porous CNTs/PDMS nanocomposites, *Nano-Micro Letters*. (2019), <https://doi.org/10.1007/s40820-019-0288-7>.
- D. Xiang, X. Zhang, Y. Li, E. Harkin-Jones, Y. Zheng, L. Wang, C. Zhao, P. Wang, Enhanced performance of 3D printed highly elastic strain sensors of carbon nanotube/thermoplastic polyurethane nanocomposites via non-covalent interactions, *Compos. B Eng.* (2019), <https://doi.org/10.1016/j.compositesb.2019.107250>.
- Y. Wang, Y. Yue, F. Cheng, Y. Cheng, B. Ge, N. Liu, Y. Gao, Ti₃C₂T_x MXene-based flexible piezoresistive physical sensors, *ACS Nano* (2022), <https://doi.org/10.1021/acsnano.1c09925>.
- Y. Lu, X. Qu, W. Zhao, Y. Ren, W. Si, W. Wang, Q. Wang, W. Huang, X. Dong, Highly stretchable, elastic, and sensitive MXene-based hydrogel for flexible strain and pressure sensors, *Research* (2020), <https://doi.org/10.34133/2020/2038560>.
- H. Liao, X. Guo, P. Wan, G. Yu, Conductive MXene nanocomposite organohydrogel for flexible, healable, low-temperature tolerant strain sensors, *Adv. Funct. Mater.* (2019), <https://doi.org/10.1002/adfm.201904507>.
- C. Xiaoyu, Z. Xuezhong, X. Dong, W. Yuanpeng, Z. Chunxia, L. Hui, L. Zhenyu, W. Ping, L. Yuntao, 3D printed high-performance spider web-like flexible strain sensors with directional strain recognition based on conductive polymer composites, *Mater. Lett.* (2021), <https://doi.org/10.1016/j.matlet.2021.130935>.
- D. Xiang, Z. Zhang, Z. Han, X. Zhang, Z. Zhou, J. Zhang, X. Luo, P. Wang, C. Zhao, Y. Li, Effects of non-covalent interactions on the properties of 3D printed flexible piezoresistive strain sensors of conductive polymer composites, *Compos. Interfaces* (2020), <https://doi.org/10.1080/09276440.2020.1794479>.
- D. Xiang, Z. Zhang, Y. Wu, J. Shen, E. Harkin-Jones, Z. Li, P. Wang, C. Zhao, H. Li, Y. Li, 3D-printed flexible piezoresistive sensors for stretching and out-of-plane forces, *Macromol. Mater. Eng.* (2021), <https://doi.org/10.1002/mame.202100437>.
- J. Kim, S.J. Park, T. Nguyen, M. Chu, J.D. Pegan, M. Khine, Highly stretchable wrinkled gold thin film wires, *Appl Phys Lett* 108 (2016) 061901.
- J. Lee, S. Kim, J. Lee, D. Yang, B.C. Park, S. Ryu, I. Park, A stretchable strain sensor based on a metal nanoparticle thin film for human motion detection, *Nanoscale* 6 (2014) 11932–11939.
- J. Shi, S. Lv, L. Wang, Z. Dai, S. Yang, L. Zhao, H. Tian, M. Du, H. Li, Y. Fang, Crack control in biotemplated gold films for wide-range, highly sensitive strain sensing, *Adv. Mater. Interfaces* 6 (2019).
- X. Junjie, H. Jingqiang, W. Weijie, C. Meimei, G. Ronghui, A multifunctional flexible strain sensor based on an excellent sensing performance PDMS-MXene@CNT/TPU nanofiber membrane with hydrophobic and photothermal conversion performance, *New J. Chem.* (2023), <https://doi.org/10.1039/d3nj03088a>.
- H. Jingqiang, L. Ang, W. Weijie, C. Ce, J. Shan, C. Meimei, Q. Wenfeng, T. Hong, G. Ronghui, Multifunctional wearable device based on an antibacterial and hydrophobic silver nanoparticles/Ti₃C₂T_x MXene/thermoplastic polyurethane fibrous membrane for electromagnetic shielding and strain sensing, *Ind. Eng. Chem. Res.* (2023), <https://doi.org/10.1021/acs.iecr.3c00214>.
- L. Ang, H. Jingqiang, W. Weijie, C. Ce, J. Shan, J. Shouxiang, Q. Wenfeng, C. Cheng, G. Ronghui, Self-heating and hydrophobic nanofiber membrane based on Ti₃C₂T_x MXene/Ag nanoparticles/thermoplastic polyurethane for electromagnetic interference shielding and sensing performance, *Ind. Eng. Chem. Res.* (2022), <https://doi.org/10.1021/acs.iecr.2c02886>.
- T.S.D. Le, H.P. Phan, S. Kwon, S. Park, Y. Jung, J. Min, B.J. Chun, H. Yoon, S.H. Ko, S.W. Kim, Y.J. Kim, Recent advances in laser-induced graphene: mechanism, fabrication, properties, and applications in flexible electronics, *Adv. Funct. Mater.* (2022), <https://doi.org/10.1002/adfm.202205158>.
- J. Zhu, X. Huang, W. Song, Physical and chemical sensors on the basis of laser-induced graphene: Mechanisms, applications, and perspectives, *ACS Nano* 15 (2021) 18708–18741.
- Z. Wan, N.-T. Nguyen, Y. Gao, Q. Li, Laser induced graphene for biosensors, *Sustain. Mater. Technol.* 25 (2020).
- L. Yang, J. Yan, C. Meng, A. Dutta, X. Chen, Y. Xue, G. Niu, Y. Wang, S. Du, P. Zhou, C. Zhang, S. Guo, H. Cheng, Vanadium oxide-doped laser-induced graphene multi-parameter sensor to decouple soil nitrogen loss and temperature, *Adv Mater* 35 (2023) e2210322.
- T. Pinheiro, S. Silvestre, J. Coelho, A.C. Marques, R. Martins, M.G.F. Sales, E. Fortunato, Laser-induced graphene on paper toward efficient fabrication of flexible, planar electrodes for electrochemical sensing, *Adv. Mater. Interfaces* 8 (2021).
- T. Pinheiro, R. Correia, M. Morais, J. Coelho, E. Fortunato, M.G.F. Sales, A. C. Marques, R. Martins, Water peel-off transfer of electronically enhanced, paper-

- based laser-induced graphene for wearable electronics, *ACS Nano* 16 (2022) 20633–20646.
- [41] T. Raza, M.K. Tufail, A. Ali, A. Boakye, X. Qi, Y. Ma, A. Ali, L. Qu, M. Tian, Wearable and flexible multifunctional sensor based on laser-induced graphene for the sports monitoring system, *ACS Appl Mater Interfaces*. (2022), <https://doi.org/10.1021/acami.2c14847>.
- [42] A. Chhetry, M. Sharifuzzaman, H. Yoon, S. Sharma, X. Xuan, J.Y. Park, MoS₂-Decorated laser-induced graphene for a highly sensitive, hysteresis-free, and reliable piezoresistive strain sensor, *ACS Appl Mater Interfaces* 11 (2019) 22531–22542.
- [43] W. Liu, Q. Chen, Y. Huang, D. Wang, L. Li, Z. Liu, In situ laser synthesis of Pt nanoparticles embedded in graphene films for wearable strain sensors with ultra-high sensitivity and stability, *Carbon* 190 (2022) 245–254.
- [44] W. Wang, L. Lu, X. Lu, Z. Liang, H. Lin, Z. Li, X. Wu, L. Lin, Y. Xie, Scorpion-inspired dual-bionic, microcrack-assisted wrinkle based laser induced graphene-silver strain sensor with high sensitivity and broad working range for wireless health monitoring system, *Nano Res.* (2022), <https://doi.org/10.1007/s12274-022-4680-0>.
- [45] Z. Pei, X. Xiong, J. He, Y. Zhang, Highly stretchable and durable conductive knitted fabrics for the skins of soft robots, *Soft Robot* 6 (2019) 687–700.
- [46] B. Kulyk, B.F.R. Silva, A.F. Carvalho, S. Silvestre, A.J.S. Fernandes, R. Martins, E. Fortunato, F.M. Costa, Laser-induced graphene from paper for mechanical sensing, *ACS Appl Mater Interfaces* 13 (2021) 10210–10221.
- [47] J. Lin, Z. Peng, Y. Liu, F. Ruiz-Zepeda, R. Ye, E.L. Samuel, M.J. Yacaman, B. I. Yakobson, J.M. Tour, Laser-induced porous graphene films from commercial polymers, *Nat Commun* 5 (2014) 5714.
- [48] C. Faugeras, A. Nerrière, M. Potemski, A. Mahmood, E. Dujardin, C. Berger, W. A. de Heer, Few-layer graphene on SiC, pyrolytic graphite, and graphene: A Raman scattering study, *Appl. Phys. Lett.* 92 (2008).
- [49] A. Reina, X. Jia, J. Ho, H. Daniel Nezhich, V. Son, M.S. Bulovic, J.K. Dresselhaus, Large area, few-layer graphene films on arbitrary substrates by chemical vapor deposition, *Nano Lett.* 9 (2008).
- [50] S.-F. Tseng, P.-S. Chen, S.-H. Hsu, W.-T. Hsiao, W.-J. Peng, Investigation of fiber laser-induced porous graphene electrodes in controlled atmospheres for ZnO nanorod-based NO₂ gas sensors, *Appl. Surf. Sci.* 620 (2023).
- [51] T. Wang, Z. Qiu, H. Li, H. Lu, Y. Gu, S. Zhu, G.S. Liu, B.R. Yang, High sensitivity, wide linear-range strain sensor based on MXene/AgNW composite film with hierarchical microcrack, *Small* (2023) e2304033, <https://doi.org/10.1002/sml.202304033>.
- [52] Z. Song, W. Li, Y. Bao, F. Han, L. Gao, J. Xu, Y. Ma, D. Han, L. Niu, Breathable and skin-mountable strain sensor with tunable stretchability, sensitivity, and linearity via surface strain delocalization for versatile skin activities' recognition, *ACS Appl Mater Interfaces* 10 (2018) 42826–42836.
- [53] W. Wang, Y. Liu, M. Ding, T. Xia, Q. Gong, X. Zeng, Z. Cai, Y. Hu, From network to channel: Crack-based strain sensors with high sensitivity, stretchability, and linearity via strain engineering, *Nano Energy* 116 (2023).
- [54] A.F. Carvalho, A.J.S. Fernandes, C. Leitão, J. Deuermeier, A.C. Marques, R. Martins, E. Fortunato, F.M. Costa, Laser-induced graphene strain sensors produced by ultraviolet irradiation of polyimide, *Adv. Funct. Mater.* 28 (2018).
- [55] A. Kaidarova, M.A. Khan, M. Marengo, L. Swanepoel, A. Przybysz, C. Muller, A. Fahlman, U. Buttner, N.R. Geraldi, R.P. Wilson, C.M. Duarte, J. Kosel, Wearable multifunctional printed graphene sensors, *npj Flexible Electron.* (2019), <https://doi.org/10.1038/s41528-019-0061-5>.
- [56] W. Liu, Y. Huang, Y. Peng, M. Walczak, D. Wang, Q. Chen, Z. Liu, L. Li, Stable wearable strain sensors on textiles by direct laser writing of graphene, *ACS Applied Nano Materials* 3 (2020) 283–293.
- [57] T. Lei, Z. Jingyu, Z. Dawei, S. Bin, Laser-induced graphene electrodes on poly (ether–ether–ketone)/PDMS composite films for flexible strain and humidity sensors, *ACS Applied Nano Materials*. (2023), <https://doi.org/10.1021/acsnm.3c03026>.
- [58] H. Wang, Z. Zhao, P. Liu, X. Guo, A soft and stretchable electronics using laser-induced graphene on polyimide/PDMS composite substrate, *npj Flexible Electron.* 6 (2022).
- [59] M. Parmeggiani, P. Zaccagnini, S. Stassi, M. Fontana, S. Bianco, C. Nicosia, C. F. Pirri, A. Lamberti, PDMS/polyimide composite as an elastomeric substrate for multifunctional laser-induced graphene electrodes, *ACS Appl Mater Interfaces* 11 (2019) 33221–33230.
- [60] A. Dallinger, K. Keller, H. Fitzek, F. Greco, Stretchable and skin-conformable conductors based on polyurethane/laser-induced graphene, *ACS Appl Mater Interfaces* 12 (2020) 19855–19865.
- [61] K. Xu, Y. Fujita, Y. Lu, S. Honda, M. Shiomi, T. Arie, S. Akita, K. Takei, A wearable body condition sensor system with wireless feedback alarm functions, *Adv Mater* 33 (2021) e2008701.
- [62] W. Jing, H. Ziyi, C. Qiushui, L. Jin-Ming, Biochemical analysis on microfluidic chips, *Trends Anal. Chem.* (2016).